Available online at www.sciencedirect.com
ScienceDirect
Journal of Computational Physics 227 (2008) 1962–1981
JOURNAL OF COMPUTATIONAL PHYSICS
www.elsevier.com/locate/jcp

Modified Smoothed Particle Hydrodynamics (MSPH) basis functions for meshless methods, and their application to axisymmetric Taylor impact test

R.C. Batra, G.M. Zhang *

Department of Engineering Science and Mechanics, MC 0219, Virginia Polytechnic Institute and State University, Blacksburg, VA 24061, United States

Received 2 October 2006; received in revised form 2 October 2007; accepted 2 October 2007
Available online 10 October 2007

Abstract

The Modified Smoothed Particle Hydrodynamics (MSPH) method proposed earlier by the authors and applied to the analysis of transient two-dimensional (2-D) heat conduction, 1-D transient simple shearing deformations of a thermoviscoplastic material, 1-D wave propagation in a functionally graded plate, and 2-D elastodynamic crack propagation is extended to the analysis of axisymmetric deformations of a thermoviscoplastic material. In the MSPH method, different shape functions are used to find kernel estimates of the function, and of its first and second derivatives. It differs from the classical finite element method in which derivatives of a function are usually obtained by differentiating the shape function used to approximate the function. It is shown that results computed with the MSPH method for the Noh problem agree well with its analytical solution. The MSPH basis functions can be used in any meshless method to numerically solve either static or dynamic problems. The method is then applied to analyze transient deformations of a cylindrical rod impacting at normal incidence a rigid smooth stationary flat plate. The computed solution is found to agree very well with those obtained by analyzing axisymmetric and 3-D transient deformations of the rod with the commercial code LS-DYNA. The final length of the deformed rod, the final radius of the impacted face, and the final length of the relatively undeformed portion of the rod for twelve test configurations computed with the MSPH method are also found to agree well with their corresponding experimental values.
Published by Elsevier Inc.

Keywords: MSPH method; Axisymmetric deformations; Taylor impact test; Thermoviscoplasticity

1. Introduction

In previous two publications [1,2] the authors proposed the modified smoothed particle hydrodynamics (MSPH) method, and applied it to analyze one-dimensional (1-D) wave propagation in an elastic bar, 2-D

* Corresponding author. Tel.: +1 540 257 3966.
E-mail address: gazhang1@vt.edu (G.M. Zhang).

0021-9991/$ - see front matter Published by Elsevier Inc.
doi:10.1016/j.jcp.2007.10.001

transient heat conduction, and 1-D transient simple shearing deformations of a thermoviscoplastic body with a defect at its center that facilitates the localization of deformation into narrow bands of intense plastic deformation. It was found that the MSPH method, without the introduction of an artificial viscosity, could accurately predict the development of severely deformed thin regions. More recently we [3,4] have used the method to study wave propagation in a functionally graded elastic plate, and crack propagation in an elastic plate subjected to time-dependent loads. The MSPH method, like its predecessor the SPH method, is total Lagrangian. We note that the SPH method was introduced by Lucy [5], and Gingold and Monaghan [6] to analyze astrophysical problems in a 3-D space. Libersky and Petschek [7] extended it to study dynamic response of materials; Monaghan [8] applied it to free surface flows, Liu et al. [9] to explosion problems, and Randles et al. [10] to impact and penetration problems. Medina and Chen [11] have enhanced the performance of the method by coupling it with parallel computing techniques.

Chen et al. [12,13] applied the concept of the kernel estimate to the Taylor series expansion of a function, called it the corrective smoothed-particle method (CSPM), and showed that it corrected the tensile instability present in the conventional SPH method; this deficiency of the SPH method and problems associated with zero energy modes have been further improved upon by Randels and Libresky [14], and Vignjevic et al. [15]. Zhang and Batra [1] modified the CSPM and by retaining terms up to second-order derivatives in the Taylor series expansion of a function introduced second-order consistency for the function, first-order consistency for the first derivative of the function, and zeroth-order consistency for the second derivative of the function. It was shown in [1] that accuracy of the computed solution improved with an increase in the order of terms retained in the Taylor series expansion. That is, for a 2-D problem involving a scalar variable (e.g. Poisson's equation), better results would be obtained by retaining second-order derivatives in the Taylor series expansion of the trial solution than by keeping only first-order derivatives. Whereas the former approach requires inverting a 6×6 matrix, in the latter alternative only a 3×3 matrix is inverted. Numerical solutions of sample problems revealed that there was no tensile instability exhibited by the MSPH method. Accordingly, we will not address consistency and tensile instability in this paper.

Here the MSPH method is extended to axisymmetric problems and is derived in cylindrical coordinates. Similarities and differences between the MSPH method and the Finite Element method (FEM) are stated. In the MSPH method, different shape functions are used to construct kernel estimates of the function (or the trial solution) and of its first and second derivatives. These shape functions are found simultaneously by solving a system of algebraic equations. However, in the FEM the shape functions are used to approximate the trial solution, and derivatives of the trial solution are obtained by differentiating the shape functions. This process usually involves inverting a matrix at each integration point within an element and thus can be computationally expensive.

Johnson [16] applied the SPH algorithm to axisymmetric geometry and divided the particle volume by the perimeter to obtain the same formula as for plane strain deformations. Petschek and Libersky [17] transformed the SPH equations from Cartesian coordinates to cylindrical coordinates and integrated them along the circumferential direction. We use Taylor series expansion of a function in cylindrical coordinates, and find kernel estimates of the function and of its derivatives by integrating equations in the circumferential direction. We illustrate the method by first analyzing the Noh problem and then deformations of a uniformly moving cylindrical rod impacting at normal incidence a smooth rigid stationary flat plate; the latter is commonly called the Taylor impact test. Results computed with the MSPH method are found to agree well with the analytical solution of the Noh problem and with those obtained from the commercial code LS-DYNA by assuming deformations to be either axisymmetric or 3-D. For twelve test configurations, the final length of the deformed rod, the diameter of the impacted face, and the final undeformed length are found to be close to their corresponding experimental values.

2. The MSPH basis functions

We use cylindrical coordinates (R,θ,Z) to analyze axisymmetric deformations of a circular cylindrical body, and note that a function, f, describing a deformation variable is independent of the angular position, θ, of a material point. Whenever convenient, we denote (R,Z) by $\mathbf{x}$ with $x_1 = R$ and $x_2 = Z$. The Taylor series expansion of a function $f(R,Z)$ about the point (R_i,Z_i) is,

$$f(R,Z) = f(R_i,Z_i) + \frac{\partial f}{\partial R}(R-R_i) + \frac{\partial f}{\partial Z}(Z-Z_i) + \frac{1}{2}\frac{\partial^2 f}{\partial R^2}(R-R_i)^2 + \frac{1}{2}\frac{\partial^2 f}{\partial Z^2}(Z-Z_i)^2 + \frac{\partial^2 f}{\partial R\partial Z}(R-R_i)(Z-Z_i) + \cdots \tag{2.1}$$

where derivatives are evaluated at the point (R_i, Z_i). Neglecting the third and higher order derivative terms on the right-hand side of Eq. (2.1), multiplying both sides of the equation with a positive-valued kernel function $W(\mathbf{x}-\xi,h)$ of compact circular support of radius $2h$ and center at the point $\mathbf{x}$, its first derivatives $W_R = \partial W/\partial R$ and $W_Z = \partial W/\partial Z$, its second derivatives $W_{RR} = \partial^2 W/\partial R^2$, $W_{ZZ} = \partial^2 W/\partial Z^2$ and $W_{RZ} = \partial^2 W/\partial R\partial Z$, and integrating the resulting equations over the domain Ω, we get,

$$\begin{aligned}
&\int_\Omega f(\boldsymbol{\xi}) W \,\mathrm{d}\boldsymbol{\xi} = f_i \int_\Omega W \,\mathrm{d}\boldsymbol{\xi} + f_{\alpha i}\int_\Omega \left(\xi_\alpha - x_\alpha^{(i)}\right) W \,\mathrm{d}\boldsymbol{\xi} + \frac{1}{2} f_{\alpha\beta i}\int_\Omega \left(\xi_\alpha - x_\alpha^{(i)}\right)\left(\xi_\beta - x_\beta^{(i)}\right) W \,\mathrm{d}\boldsymbol{\xi},\\
&\int_\Omega f(\boldsymbol{\xi}) W_R \,\mathrm{d}\boldsymbol{\xi} = f_i \int_\Omega W_R \,\mathrm{d}\boldsymbol{\xi} + f_{\alpha i}\int_\Omega \left(\xi_\alpha - x_\alpha^{(i)}\right) W_R \,\mathrm{d}\boldsymbol{\xi} + \frac{1}{2} f_{\alpha\beta i}\int_\Omega \left(\xi_\alpha - x_\alpha^{(i)}\right)\left(\xi_\beta - x_\beta^{(i)}\right) W_R \,\mathrm{d}\boldsymbol{\xi},\\
&\int_\Omega f(\boldsymbol{\xi}) W_Z \,\mathrm{d}\boldsymbol{\xi} = f_i \int_\Omega W_Z \,\mathrm{d}\boldsymbol{\xi} + f_{\alpha i}\int_\Omega \left(\xi_\alpha - x_\alpha^{(i)}\right) W_Z \,\mathrm{d}\boldsymbol{\xi} + \frac{1}{2} f_{\alpha\beta i}\int_\Omega \left(\xi_\alpha - x_\alpha^{(i)}\right)\left(\xi_\beta - x_\beta^{(i)}\right) W_Z \,\mathrm{d}\boldsymbol{\xi},\\
&\int_\Omega f(\boldsymbol{\xi}) W_{RR} \,\mathrm{d}\boldsymbol{\xi} = f_i \int_\Omega W_{RR} \,\mathrm{d}\boldsymbol{\xi} + f_{\alpha i}\int_\Omega \left(\xi_\alpha - x_\alpha^{(i)}\right) W_{RR} \,\mathrm{d}\boldsymbol{\xi} + \frac{1}{2} f_{\alpha\beta i}\int_\Omega \left(\xi_\alpha - x_\alpha^{(i)}\right)\left(\xi_\beta - x_\beta^{(i)}\right) W_{RR} \,\mathrm{d}\boldsymbol{\xi},\\
&\int_\Omega f(\boldsymbol{\xi}) W_{ZZ} \,\mathrm{d}\boldsymbol{\xi} = f_i \int_\Omega W_{ZZ} \,\mathrm{d}\boldsymbol{\xi} + f_{\alpha i}\int_\Omega \left(\xi_\alpha - x_\alpha^{(i)}\right) W_{ZZ} \,\mathrm{d}\boldsymbol{\xi} + \frac{1}{2} f_{\alpha\beta i}\int_\Omega \left(\xi_\alpha - x_\alpha^{(i)}\right)\left(\xi_\beta - x_\beta^{(i)}\right) W_{ZZ} \,\mathrm{d}\boldsymbol{\xi},\\
&\int_\Omega f(\boldsymbol{\xi}) W_{RZ} \,\mathrm{d}\boldsymbol{\xi} = f_i \int_\Omega W_{RZ} \,\mathrm{d}\boldsymbol{\xi} + f_{\alpha i}\int_\Omega \left(\xi_\alpha - x_\alpha^{(i)}\right) W_{RZ} d\boldsymbol{\xi} + \frac{1}{2} f_{\alpha\beta i}\int_\Omega \left(\xi_\alpha - x_\alpha^{(i)}\right)\left(\xi_\beta - x_\beta^{(i)}\right) W_{RZ} \,\mathrm{d}\boldsymbol{\xi},
\end{aligned} \tag{2.2}$$

where $f_i = f(\mathbf{x}^{(i)})$, $f_{\alpha i} = \partial f/\partial x_\alpha^{(i)}$, and $f_{\alpha\beta i} = \partial^2 f/\partial x_\alpha^{(i)}\partial x_\beta^{(i)}$, α, $\beta = 1,2$ and $x_1 = R, x_2 = Z$. Because the kernel function W is zero when the distance $|\mathbf{x}-\boldsymbol{\xi}|$ is greater than $2h$ (h is the smoothing length), the integration domain Ω can be replaced by the compact support of the kernel function. Eqs. (2.2) can be written in matrix form as

$$BF = T \quad \text{or } B_{IJ}F_J = T_I, \quad I = 1,2,\ldots 6, \tag{2.3}$$

where

$$\begin{aligned}
&B_{IJ} = \int_\Omega \Phi(I)\Theta(J)\,\mathrm{d}\xi = \sum_{j=1}^{N} \Phi(I)\Theta(J)\frac{m_j}{\rho_j},\\
&\Phi(1) = W_{ij}, \quad \Phi(2) = W_{ij,1}, \quad \Phi(3) = W_{ij,2},\\
&\Phi(4) = W_{ij,11}, \quad \Phi(5) = W_{ij,22}, \quad \Phi(6) = W_{ij,12},\\
&\Theta(1) = 1, \quad \Theta(2) = R_j - R_i, \quad \Theta(3) = Z_j - Z_i,\\
&\Theta(4) = \frac{1}{2}(R_j - R_i)^2, \quad \Theta(5) = \frac{1}{2}(Z_j - Z_i)^2, \quad \Theta(6) = (R_j - R_i)(Z_j - Z_i),\\
&F = \{f_i, f_{1i}, f_{2i}, f_{11i}, f_{22i}, f_{12i}\}^{\mathrm{T}},\\
&T_I = \int_\Omega f(\boldsymbol{\xi})\Phi(I)\,\mathrm{d}\boldsymbol{\xi} = \sum_{j=1}^{N} f_j \Phi(I)\frac{m_j}{\rho_j},\\
&W_{ij} = W\left(\mathbf{x}^{(i)} - \boldsymbol{\xi}^{(j)}, h\right),\\
&W_{ij,\alpha} = \left.\frac{\partial W}{\partial x_\alpha}\right|_{\mathbf{x}=\mathbf{x}^{(i)},\boldsymbol{\xi}=\boldsymbol{\xi}^{(j)}}, \quad W_{ij,\alpha\beta} = \left.\frac{\partial^2 W}{\partial x_\alpha \partial x_\beta}\right|_{\mathbf{x}=\mathbf{x}^{(i)},\boldsymbol{\xi}=\boldsymbol{\xi}^{(j)}}.
\end{aligned} \tag{2.4}$$

Here N equals the number of particles located in the compact support of the kernel function $W(\mathbf{x}-\boldsymbol{\xi},h)$. These equations are the same as those in plane strain problems except that the mass, m_j, now equals the mass of a circular ring rather than that of a cylinder of unit length.

If N equals at least six and particles are randomly distributed in the compact support of the kernel function, then the determinant of matrix B is nonzero and Eq. (2.3) can be rewritten as

$$F_J = B_{IJ}^{-1} T_I, \tag{2.5}$$

where $^{-1}$ denotes the inverse of a matrix. Eq. (2.5) gives values of the function f and of its first-order and second-order derivatives at the point $\mathbf{x}$ in terms of values of f at points in the neighborhood of$\mathbf{x}$; the number N of these points is determined by the radius, $2h$, of the compact support of the kernel function W. Eq. (2.5) can be explicitly written as

$$\begin{aligned} f(\mathbf{x}) &= B_{I1} T_I = \sum_{J=1}^{N} B_{I1}\Phi(I)\frac{m_J}{\rho_J} f_J, \\ \frac{\partial f(\mathbf{x})}{\partial x_1} &= B_{I2} T_I = \sum_{J=1}^{N} B_{I2}\Phi(I)\frac{m_J}{\rho_J} f_J, \\ \frac{\partial^2 f(\mathbf{x})}{\partial x_1^2} &= B_{I4} T_I = \sum_{J=1}^{N} B_{I4}\Phi(I)\frac{m_J}{\rho_J} f_J. \end{aligned} \tag{2.6}$$

In the terminology of the FEM functions $B_{I1}\Phi(I)\frac{m_J}{\rho_J}, I = 1,2,\ldots,6$ *can be viewed as shape functions for the function* f. Similarly, functions $B_{I2}\Phi(I)\frac{m_J}{\rho_J}, I = 1,2,\ldots,6$ and $B_{I4}\Phi(I)\frac{m_J}{\rho_J}, I = 1,2,\ldots,6$ *can be regarded as shape functions for* $\partial f(\mathbf{x})/\partial x_1$ and $\partial^2 f(\mathbf{x})/\partial x_1^2$ *respectively*. Thus shape functions for $f(\mathbf{x})$, its first derivative and its second derivative at the point $\mathbf{x}$ are different. Recall that in the FEM

$$\frac{\partial^{\alpha+\beta+\gamma}}{\partial x_1^\alpha \partial x_2^\beta \partial x_3^\gamma} f(\mathbf{x}) = \sum_{J=1}^{N} \frac{\partial^{\alpha+\beta+\gamma}}{\partial x_1^\alpha \partial x_2^\beta \partial x_3^\gamma} N_J f_J. \tag{2.7}$$

For $\alpha = \beta = \gamma = 0$, Eq. (2.7) giving the approximate value of the function in the FEM is exactly of the same form as that in the MSPH method. Of course, shape functions for the MSPH and the FEM are different. Also expressions for approximate values of the first and the second derivatives of the function at the point $\mathbf{x}$ in the MSPH method are different from those in the FEM. In order to compute approximate values of derivatives of the function in the MSPH method, we do not need to differentiate the basis functions. Instead we use another set of basis functions. Values of coefficients in Eq. (2.6) for finding approximate values of the function $f(\mathbf{x})$, its first derivative and its second derivative at the point $\mathbf{x}$ are determined simultaneously.

It is clearly seen that for the MSPH method, kernel estimates of the second derivatives, first derivative and the function are consistent of orders $(n-2)$, $(n-1)$ and n, respectively, if up to n order terms are retained in the Taylor series expansion, Eq. (2.1).

We use the following revised Gauss function $W(\mathbf{x}-\boldsymbol{\xi},h)$ as the kernel function:

$$W(\mathbf{x}-\boldsymbol{\xi},h) = \begin{cases} \frac{1.10081}{(h\sqrt{\pi})^2}\left(\mathrm{e}^{-|\mathbf{x}-\boldsymbol{\xi}|^2/h^2} - \mathrm{e}^{-4}\right) & |\mathbf{x}-\boldsymbol{\xi}| \leqslant 2h, \\ 0 & |\mathbf{x}-\boldsymbol{\xi}| > 2h, \end{cases} \tag{2.8}$$

and note that the integral of $W(\mathbf{x}-\boldsymbol{\xi},h)$ over its compact support equals one.

3. Governing equations

In cylindrical coordinates, equations expressing the conservation of mass, the conservation of linear momentum, and the conservation of internal energy for axisymmetric deformations are

$$\frac{\mathrm{d}\rho}{\mathrm{d}t} = -\rho\left(\frac{\partial U_R}{\partial R} + \frac{U_R}{R} + \frac{\partial U_Z}{\partial Z}\right), \tag{3.1}$$

$$\frac{\mathrm{d}U_R}{\mathrm{d}t} = \frac{1}{\rho}\left[\frac{\partial \sigma_{RR}}{\partial R} + \frac{1}{R}(\sigma_{RR} - \sigma_{\theta\theta}) + \frac{\partial \sigma_{RZ}}{\partial Z}\right], \tag{3.2}$$

$$\frac{\mathrm{d}U_Z}{\mathrm{d}t} = \frac{1}{\rho}\left[\frac{\partial \sigma_{RZ}}{\partial R} + \frac{1}{R}\sigma_{RZ} + \frac{\partial \sigma_{ZZ}}{\partial Z}\right], \tag{3.3}$$

$$\rho\dot{e} = \mathrm{tr}(\boldsymbol{\sigma}\mathbf{D}). \tag{3.4}$$

Here ρ denotes the mass density of a material particle, $\mathbf{U}$ its velocity, $\mathrm{d}/\mathrm{d}t$ or a superimposed dot the total derivative with respect to time t, $\boldsymbol{\sigma}$ the Cauchy stress tensor, e the specific internal energy, $\mathbf{D}$ the strain-rate tensor, and tr( ) is the trace operator. When the R coordinate approaches zero, Eqs. (3.1)–(3.3) are no longer valid, and using L'Hospital's rule they become

$$\frac{\mathrm{d}\rho}{\mathrm{d}t} = -\rho\left(2\frac{\partial U_R}{\partial R} + \frac{\partial U_Z}{\partial Z}\right),$$
$$U_R = 0,$$
$$\frac{\mathrm{d}U_Z}{\mathrm{d}t} = \frac{1}{\rho}\left[2\frac{\partial \sigma_{RZ}}{\partial R} + \frac{\partial \sigma_{ZZ}}{\partial Z}\right].$$

In Eq. (3.4) deformations have been assumed to be locally adiabatic, thus effects of heat conduction have been neglected. This assumption is reasonable for studying the short time response in a transient problem such as deformations occurring in a Taylor impact test unless one is interested in finding the width of the region of intense plastic deformations; e.g. see [26,27]. We assume that the rate of change of internal energy is related to the rate of change of temperature through the relation

$$\rho\dot{e} = \rho C\dot{T} + \mathrm{tr}(\boldsymbol{\sigma}\mathbf{D}^{\mathrm{e}}), \tag{3.5}$$

where C is the specific heat, T the present temperature of a material point, and $\mathbf{D}^{\mathrm{e}}$ the elastic part of the strain-rate tensor.

Substitution from Eq. (3.5) into Eq. (3.4) yields the following equation for the rate of change of temperature

$$\rho C\dot{T} = \mathrm{tr}(\boldsymbol{\sigma}\mathbf{D} - \boldsymbol{\sigma}\mathbf{D}^{\mathrm{e}}) = \mathrm{tr}(\boldsymbol{\sigma}\mathbf{D}^{\mathrm{p}}), \tag{3.6}$$

where $\mathbf{D}^{\mathrm{p}}$ equals the plastic part of the strain-rate tensor. Eqs. (3.1)–(3.6) need to be supplemented by constitutive relations, initial conditions, and boundary conditions.

The thermo-visco-plastic response of the material is assumed to be represented by the following empirical Johnson-Cook relation that considers strain hardening, strain-rate hardening, and thermal softening effects.

$$\sigma_Y = (a + b(\varepsilon^{\mathrm{p}})^n)\left(1 + c\ln\left(\frac{\dot{\varepsilon}}{\dot{\varepsilon}_0}\right)\right)(1 - T^{*m}). \tag{3.7}$$

Here σ_Y is the flow stress of the material; b, n and c are the strain hardening coefficient, the strain hardening exponent, and the strain-rate hardening parameter, respectively, and $\dot{\varepsilon}_0$ is the reference strain rate. $T^* = \frac{T - T_{\mathrm{room}}}{T_{\mathrm{M}} - T_{\mathrm{room}}}$, where T_{M} is the fictitious melting temperature of the material obtained by fitting a curve by the least squares method to the test data, T the current temperature, T_{room} the room temperature, and m the thermal softening exponent. The effective strain rate $\dot{\varepsilon}$ is given by

$$\dot{\varepsilon} = \sqrt{D_{ij}D_{ij}}. \tag{3.8}$$

The Jaumann rate of the deviatoric stress, $S^{\nabla}_{\alpha\beta}$, defined by

$$S^{\nabla}_{\alpha\beta} = \dot{S}_{\alpha\beta} - S_{\alpha\gamma}\dot{R}_{\beta\gamma} - S_{\gamma\beta}\dot{R}_{\alpha\gamma}, \tag{3.9}$$

is computed from

$$S^{\nabla}_{\alpha\beta} = 2\mu\left(D_{\alpha\beta} - \frac{1}{3}\delta_{\alpha\beta}\dot{\varepsilon}_{\mathrm{V}}\right), \tag{3.10}$$

where $\dot{\varepsilon}_{\mathrm{V}} = D_{ii}$ is the volumetric strain rate, μ the shear modulus, and $\delta_{\alpha\beta}$ the Kronecker delta. The components of the strain rate tensor $\mathbf{D}$ and the spin tensor $\dot{\boldsymbol{R}}$ in rectangular Cartesian coordinates are given by

$$D_{\alpha\beta} = \frac{1}{2}\left(\frac{\partial U_\alpha}{\partial x_\beta} + \frac{\partial U_\beta}{\partial x_\alpha}\right),$$
$$\dot{R}_{\alpha\beta} = \frac{1}{2}\left(\frac{\partial U_\alpha}{\partial x_\beta} - \frac{\partial U_\beta}{\partial x_\alpha}\right).$$

Physical components of **D** in cylindrical coordinates are

$$D_{RR}=\frac{\partial U_R}{\partial R},\quad D_{RZ}=\frac{1}{2}\left(\frac{\partial U_R}{\partial Z}+\frac{\partial U_Z}{\partial R}\right),\quad D_{\theta\theta}=\frac{U_R}{R},\quad D_{ZZ}=\frac{\partial U_Z}{\partial Z}.$$

We compute stresses at time $t_n+\mathrm{d}t$ by assuming that deformations during the time interval $(t_n, t_n+\mathrm{d}t)$ are elastic and subsequently correct them if the resulting stresses lie outside the yield surface. Thus the trial deviatoric stress, $S^*_{\alpha\beta}$, at time $t_n+\mathrm{d}t$ is given by

$$S^*_{\alpha\beta}=S^n_{\alpha\beta}+\left[S_{\alpha\gamma}\dot{R}_{\beta\gamma}+S_{\gamma\beta}\dot{R}_{\alpha\gamma}+2\mu\left(\dot{D}_{\alpha\beta}-\frac{1}{3}\dot{\varepsilon}_V\delta_{\alpha\beta}\right)\right]\mathrm{d}t. \tag{3.11}$$

The only nonzero component of $\dot{\boldsymbol{R}}$ in cylindrical coordinates is $\dot{R}_{RZ}$ that equals $\frac{1}{2}(\frac{\partial U_R}{\partial Z}-\frac{\partial U_Z}{\partial R})$. The final deviatoric stress at time $t_n+\mathrm{d}t$ is the trial deviatoric stress $S^*_{\alpha\beta}$ if

$$\frac{1}{2}S^*_{ij}S^*_{ij}-\frac{1}{3}\sigma_y^2\leqslant 0. \tag{3.12}$$

Otherwise, we scale the trial deviatoric stresses back to the yield surface by

$$S^{n+1}_{\alpha\beta}=\frac{\sigma_y}{\sqrt{\frac{3}{2}S^*_{ij}S^*_{ij}}}S^*_{\alpha\beta}. \tag{3.13}$$

Note that Eq. (3.12) with the equality sign is the von Mises yield surface. We define the equivalent stress by

$$S^*=\sqrt{\frac{3}{2}S^*_{ij}S^*_{ij}} \tag{3.14}$$

and introduce the function

$$\hat{f}=\min\left(\sigma_y/S^*,1\right). \tag{3.15}$$

From Eqs. (3.13)–(3.15), the deviatoric stress $S^{n+1}_{\alpha\beta}$ at the time $t_n+\mathrm{d}t$ can be expressed as

$$S^{n+1}_{\alpha\beta}=\hat{f}S^*_{\alpha\beta}. \tag{3.16}$$

The pressure is assumed to change linearly with the compression ratio, i.e.,

$$P=K\left(\frac{\rho}{\rho_0}-1\right), \tag{3.17}$$

where K is the bulk modulus. After the deviatoric stress and the pressure at time t_{n+1} have been computed, we get the stress tensor at time $t_n+\mathrm{d}t$ from

$$\sigma^{n+1}_{\alpha\beta}=-P^{n+1}\delta_{\alpha\beta}+S^{n+1}_{\alpha\beta}. \tag{3.18}$$

The increment in the deviatoric strain tensor equals $(D_{\alpha\beta}-\frac{1}{3}\dot{\varepsilon}_V\delta_{\alpha\beta})\,\mathrm{d}t$, and the elastic part of the deviatoric strain increment $\Delta\bar{\varepsilon}^{\mathrm{e}}_{\alpha\beta}$ is given by

$$\Delta\bar{\varepsilon}^{\mathrm{e}}_{\alpha\beta}=\left(S^{n+1}_{\alpha\beta}-\left(S^n_{\alpha\beta}+S_{\alpha\gamma}\dot{R}_{\beta\gamma}+S_{\gamma\beta}\dot{R}_{\alpha\gamma}\right)\mathrm{d}t\right)\Big/2\mu. \tag{3.19}$$

From Eqs. (3.10), (3.11) and (3.19), we find that the plastic strain increment is given by

$$\Delta\varepsilon^{\mathrm{p}}_{\alpha\beta}=\Delta\bar{\varepsilon}_{\alpha\beta}-\Delta\bar{\varepsilon}^{\mathrm{e}}_{\alpha\beta}=\left(S^*_{\alpha\beta}-S^{n+1}_{\alpha\beta}\right)/2\mu=\left(1-\hat{f}\right)S^*_{\alpha\beta}/2\mu. \tag{3.20}$$

After having found all components of the plastic strain increment, we compute the effective plastic strain increment from

$$\Delta\varepsilon^{\mathrm{p}}=\sqrt{\frac{2}{3}\Delta\varepsilon^{\mathrm{p}}_{ij}\Delta\varepsilon^{\mathrm{p}}_{ij}}=\frac{1}{3}\frac{1-\hat{f}}{\mu}S^*. \tag{3.21}$$

We replace the function $f(R,Z)$ in Eq. (2.2) by U_R, U_Z, σ_{RR}, etc., and solve the resulting system of Eq. (2.3) for terms involving derivatives on the right-hand sides of Eqs. (3.1)–(3.3) in terms of values of $\boldsymbol{U}$ and $\boldsymbol{\sigma}$ at points in the neighborhood of the point $\mathbf{x}$. This procedure is repeated for suitably scattered points or particles $\mathbf{x}$ in the domain Ω. We thus arrive at a set of coupled nonlinear ordinary differential equations (ODEs) expressing time derivatives of ρ and $\mathbf{U}$ in terms of values of ρ, $\mathbf{U}$ and $\boldsymbol{\sigma}$ at discrete points in Ω. Knowing the constitutive relation characterizing the response of the material that expresses stresses in terms of velocity gradients, these ODEs are integrated with respect to time t by the central-difference method.

The time step $\mathrm{d}t_i$ of particle i is determined from the Courant–Fredrich–Levy condition

$$\mathrm{d}t_i = 0.2\frac{h_i}{c_i + |\mathbf{U}_i|}, \tag{3.22}$$

where h_i, c_i and $\mathbf{U}_i$ are the smoothing length, the sound speed, and the velocity vector, of particle i, respectively. The time step used to integrate coupled ODEs equals the minimum of the time steps for all particles.

In order to control oscillations near the shock wave, the conservative smoothing method [18–21] is often applied to smooth out the density and the velocity fields. Conservative smoothing removes tensile instability, but it sometimes also eliminates fine details of the solution. Hicks and Liebrock [22] have shown that for 1-D problems the SPH B-spline finite interpolation method can stabilize the solution without excessive loss of its fine details. It is not known whether the method can be extended to 2-D problems. It seems that with some modifications, the procedure should also work for 2-D and 3-D problems. However, this is not the focus of our work. For problems involving shock loads, conservative smoothing can yield larger stable time steps and less error in the approximate solution than those when the artificial viscosity is used. The smoothing function is defined by

$$g(f_i,\alpha_{\mathrm{cs}}) = f_i + \alpha_{\mathrm{cs}}\left[\frac{\sum_{j=1}^{N} f_j W_{ij} m_j/\rho_j}{\sum_{j=1}^{N} W_{ij} m_j/\rho_j} - f_i\right]. \tag{3.23}$$

The coefficient α_{cs} that satisfies $0 < \alpha_{\mathrm{cs}} \leqslant 0.5$ is taken as 0.3 in this work. At each time step, after the density and the velocity fields have been computed from Eqs. (3.1)–(3.3), they are smoothened with Eq. (3.23).

4. Results and discussion

4.1. Noh's problem

Before presenting numerical results for the Taylor impact test, we use the MSPH method to solve Noh's problem [23] in cylindrical coordinates. Conservation equations and constitutive relations for Noh's problem for a gas are

$$\frac{\mathrm{d}\rho}{\mathrm{d}t} = -\rho\left(\frac{\partial U_R}{\partial R} + \frac{U_R}{R}\right), \tag{4.1}$$

$$\frac{\mathrm{d}U_R}{\mathrm{d}t} = -\frac{1}{\rho}\frac{\partial P}{\partial R}, \tag{4.2}$$

$$\frac{\mathrm{d}e}{\mathrm{d}t} = -\frac{P}{\rho}\left(\frac{\partial U_R}{\partial R} + \frac{U_R}{R}\right), \tag{4.3}$$

$$P = (\gamma - 1)\rho e. \tag{4.4}$$

Here, P is the gas pressure, and γ the specific heat. For an ideal gas, we set $\gamma = 5/3$, mass density $\rho = 1$, and assume that it moves in the radial direction. The initial conditions are:

$$U_R(R) = \begin{cases} -1 & 1 \geqslant R > 0, \\ 0 & R = 0, \end{cases}$$

$$e = 0; \quad P = 0; \quad \rho = 1.$$

The analytical solution gives that a shock moves radially outwards with velocity = 1/3. The density, the pressure, the velocity and the specific energy behind the shock are 16, 16/3, 0 and 0.5, while they are $1 + t/R$, 0, -1 and 0 in front of the shock where t is the time. The distributions of the mass density, the pressure, the velocity and the specific energy at t = 0.6 computed with the MSPH method using 800 uniformly distributed particles are depicted in Fig. 1. The analytical solutions (solid line) are also plotted in Fig. 1 for easy comparison with the numerical solution. It can be seen that the MSPH method captures the shock well, and the computed results agree well with the corresponding analytical ones except near the cylinder center where the computed energy (mass density) is much higher (lower) than its analytical value. This can be alleviated by introducing an artificial heat conduction term in the energy equation, but has not been pursued here.

4.2. Taylor impact

We first analyze transient deformations of a 37.97 mm long and 7.595 mm diameter cylindrical rod made of low strength 4340 steel, and striking a rigid stationary smooth anvil at normal incidence with a speed of

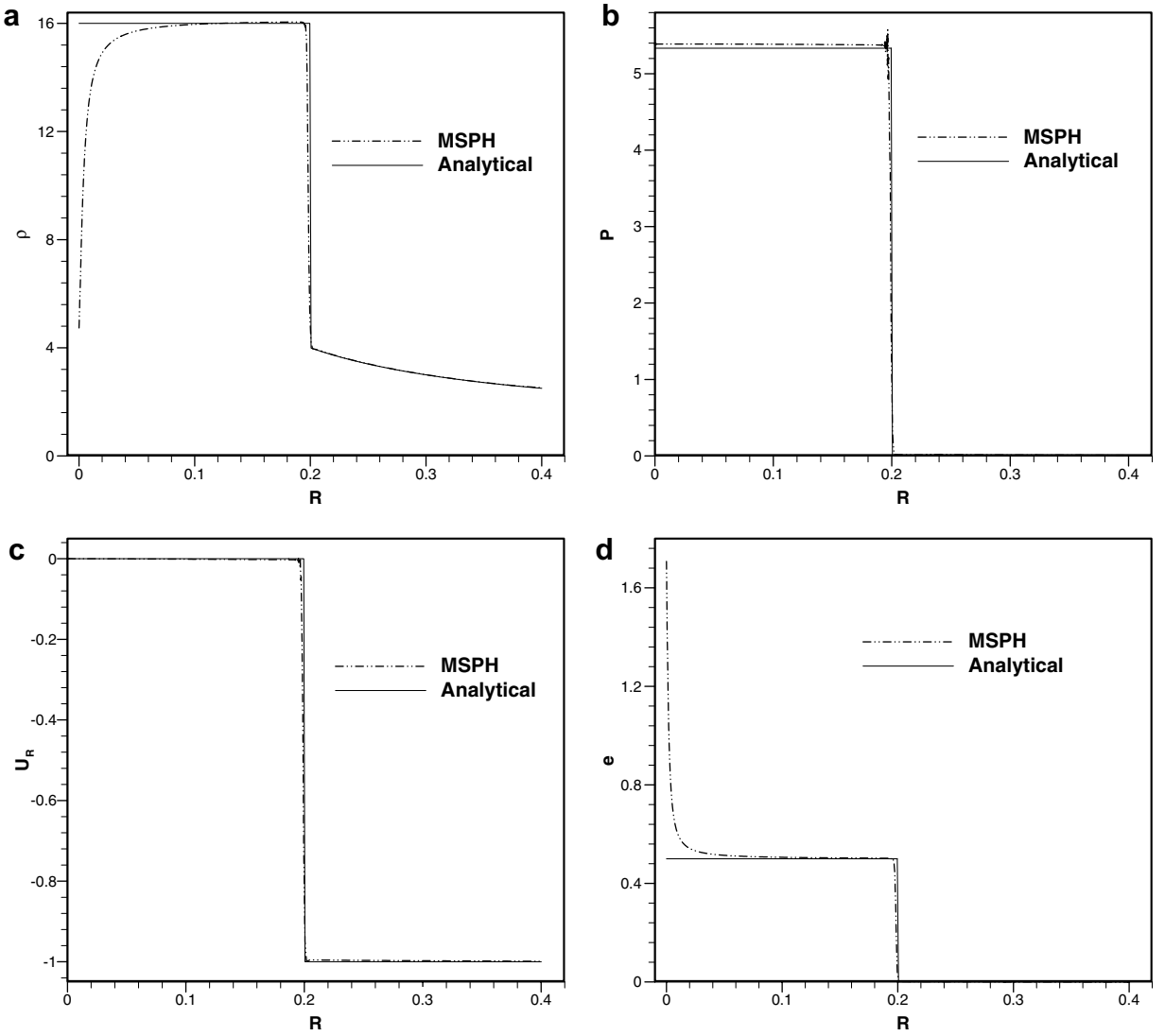

Fig. 1. Comparison of the MSPH solution for the distributions of (a) the density, (b) the pressure, (c) the radial velocity, and (d) the specific energy computed with the MSPH method with those from the analytical solution.

181 m/s. We compare computed results with the experimental findings of House and Lewis [24], and also with numerical solutions obtained by using the commercial code LS-DYNA. Values assigned to different material parameters [25] are

$$\rho = 7830\ \text{kg/m}^3, \quad \mu = 82.9\ \text{GPa}, \quad K = 169.1\ \text{GPa}, \quad C = 460\ \text{J/Kg K},$$
$$a = 792\ \text{MPa}, \quad b = 510\ \text{MPa}, \quad n = 0.26, \quad c = 0.014, \quad \text{m} = 1.03,$$
$$T_{\text{M}} = 1293\ \text{K}, \quad T_{\text{room}} = 293\ \text{K}, \quad \dot{\varepsilon}_0 = 1/s.$$

A total of 3820 particles with 20 in the radial and 191 in the axial directions are uniformly placed in the region occupied by the rod in the reference configuration; thus the distance between adjacent particles in the radial direction equals that in the axial direction. The initial smoothing length, h, is taken as 1.5 times the distance between adjacent particles, Δ. The rod is assumed to be initially stress free, at room temperature and moving with a uniform velocity in the axial direction. During deformations of the rod, its mantle (cylin-

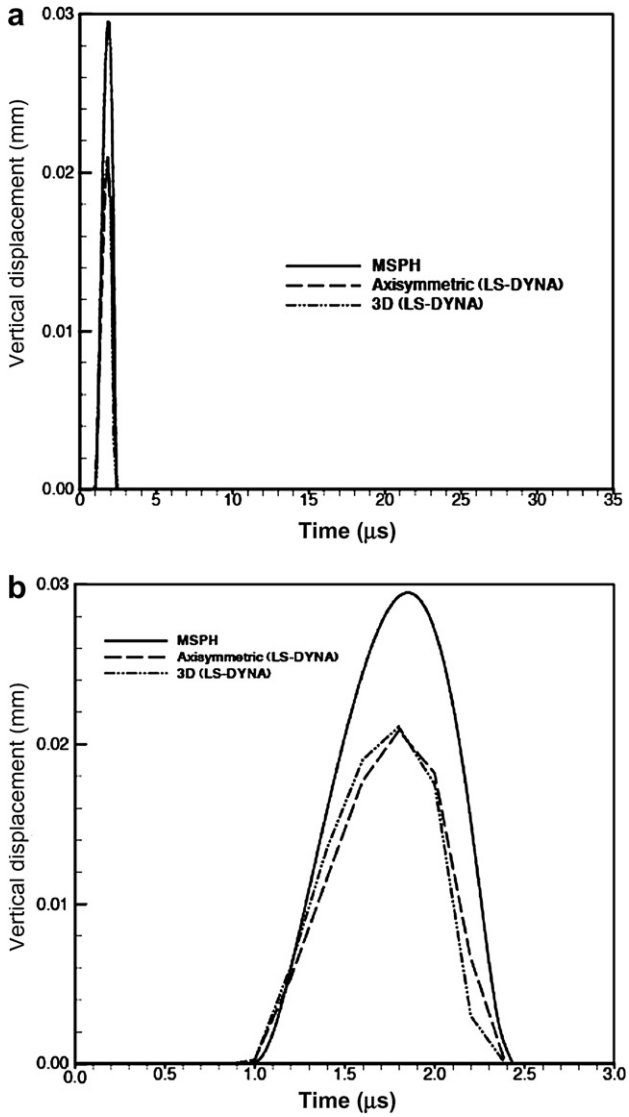

Fig. 2. Time histories of the vertical displacement of the centroid of the impact face computed with the MSPH code, and the axisymmetric and the 3-D analyses with LS-DYNA.

drical surface) and top surface are taken to be traction free and thermally insulated, and the contact surface between the rod and the immovable flat anvil to be smooth and thermally insulated. The traction free boundary conditions are imposed by first transforming the stress tensor at a boundary point into local coordinates with axes aligned along and perpendicular to the boundary surface, and then setting the normal and the tangential tractions equal to zero. The stress tensor is then transformed back to the global coordinate axes. Essential boundary conditions at points on the impact face and on the centroidal axis of the bar are satisfied by setting the appropriate component of velocity equal to its prescribed value. The thermal boundary condition of bounding surfaces being thermally insulated is automatically satisfied since deformations have been taken to be locally adiabatic. The time is reckoned from the instant of impact. If a part of rod's impact face leaves the anvil surface, then it is taken to be traction free and thermally insulated. Since the impacted face cannot

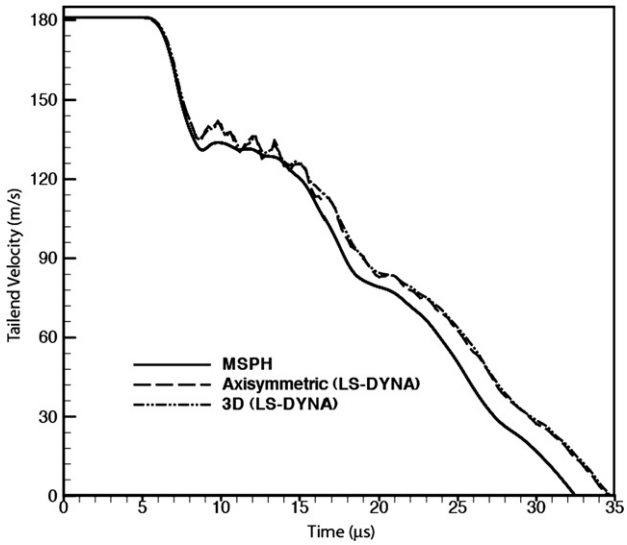

Fig. 3. Time history of the tail end axial velocity computed with the MSPH code, and the axisymmetric (LS-DYNA) and the 3-D LS-DYNA (LS-DYNA) analyses.

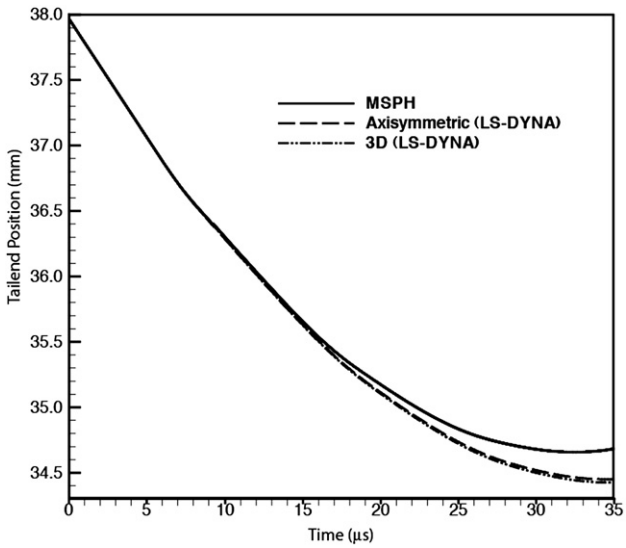

Fig. 4. Time histories of the rod length for the three analyses.

sustain tensile normal traction, when the stress component σ_{ZZ} at a point on rod's impact surface is tensile, the traction free boundary condition at that point is enforced and the point is taken to have lost contact with the anvil.

Results computed with the MSPH method are compared with those obtained by using the commercial FE code LS-DYNA and by assuming that deformations are either axisymmetric or 3-D. Coordinates of nodes in the FE mesh are the same as those of particles in the MSPH method. For axisymmetric analysis with

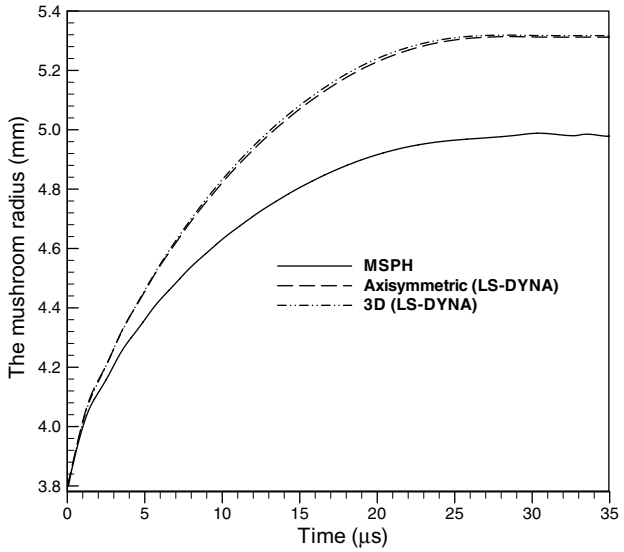

Fig. 5. Time histories of the radius of the impacted face of the rod for the three analyses.

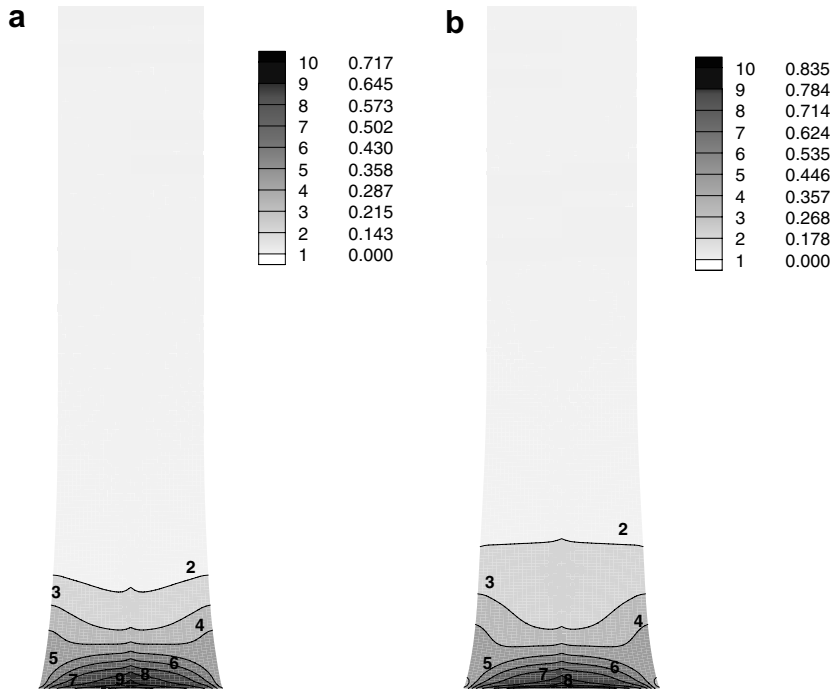

Fig. 6. Contours of the effective plastic strain in the rod at (a) 15 μs and (b) 30 μs computed by the MSPH method.

LS-DYNA, the number of nodes and elements are 3820 and 3610, while for the 3-D analysis there are 65,550 nodes and 72,580 hexahedron elements. The FE discretizations in the RZ-plane for the axisymmetric and the 3-D analyses are identical.

Fig. 2a depicts time histories of the position of the material particle initially at the center of the impact face as computed by the MSPH method, and the two analyses with LS-DYNA; results for $0 \leqslant t \leqslant 3.0$ μs are shown in Fig. 2b. The two solutions with LS-DYNA are identical implying that deformations are indeed axisymmetric as expected. The center of the impact surface does not leave the anvil until about 1.0 μs. The gap between the center of the impact surface and the anvil increases, reaches a maximum, and subsequently decreases. The maximum upward displacement of the particle given by the MSPH method is 0.03 mm, while that by the LS-DYNA is 0.02 mm. However both codes predict that the material point at the centroid of the impact face re-establishes contact with the anvil at 2.4 μs.

Time histories of the axial velocity of a material particle at the center of the free end face, or the tail end of the rod, are exhibited in Fig. 3. The speed of the elastic wave is given by $C_e = \sqrt{\frac{K+4\mu/3}{\rho}} = 5976$ m/s, and it will arrive at the tail end at time $t = L/C_e = 6.3$ μs. Each one of the three analyses predicts that the speed of the tail end begins to decrease at $t \approx 6.3$ μs. The solution given by LS-DYNA exhibits oscillations after the speed

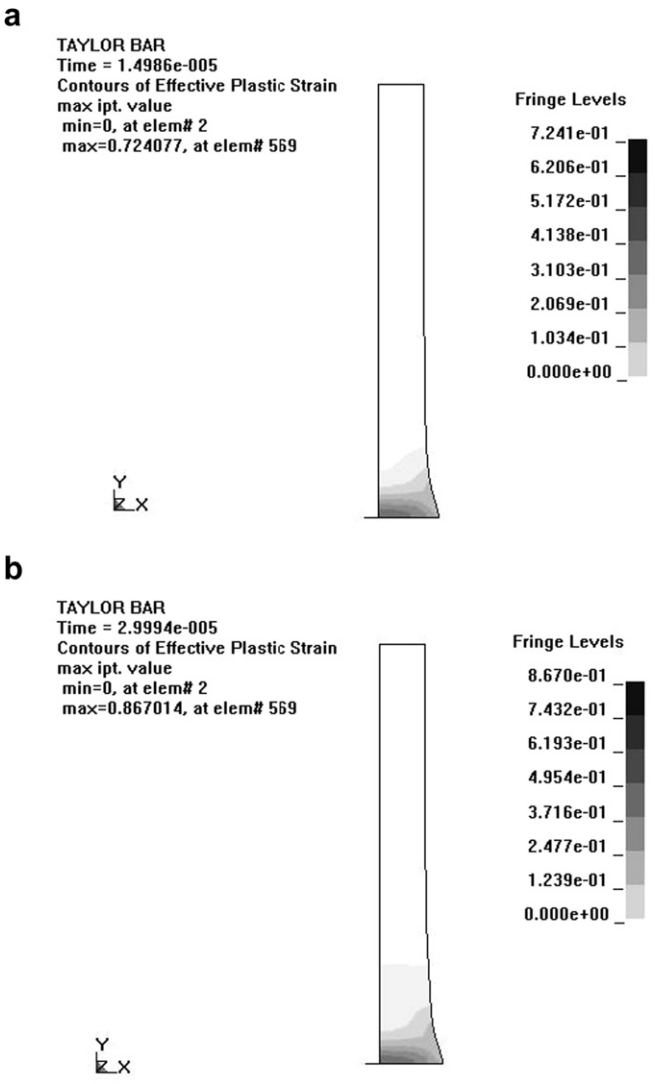

Fig. 7. Fringe plots of the effective plastic strain in the rod at (a) 15 μs and (b) 30 μs computed with the LS-DYNA code.

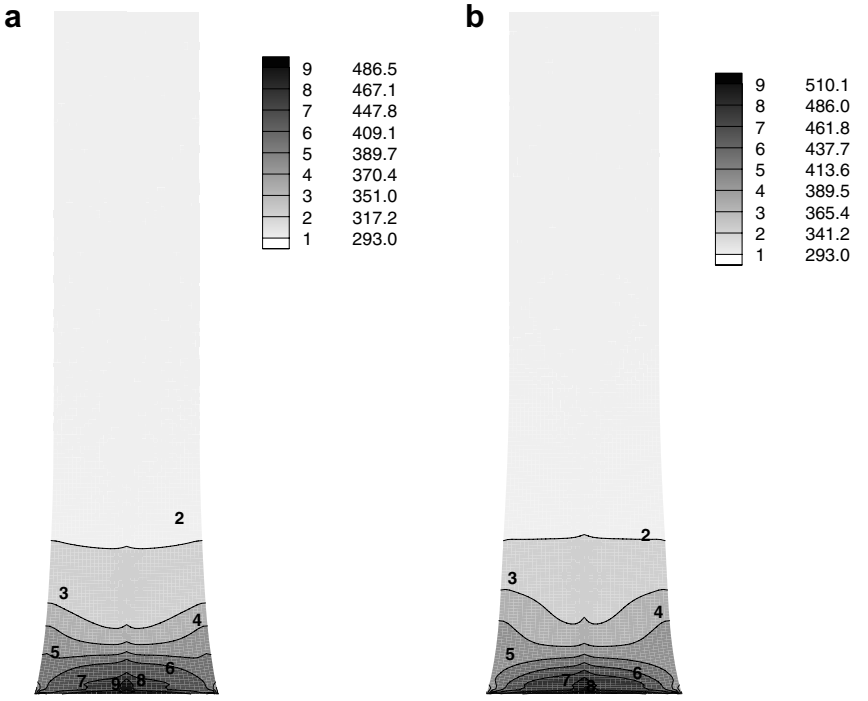

Fig. 8. Contours of the temperature in the rod at time (a) 15 μs and (b) 30 μs computed with the MSPH method.

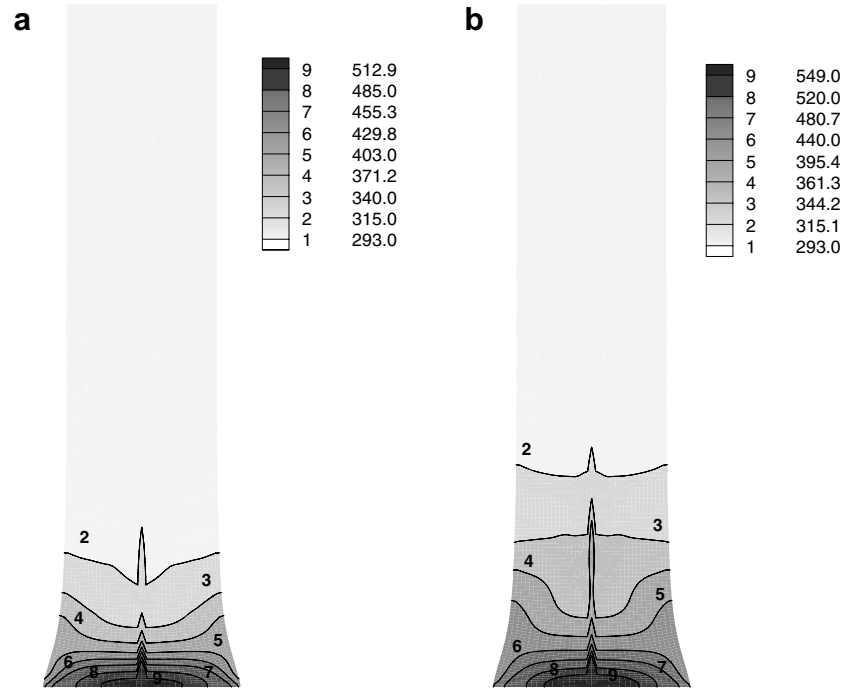

Fig. 9. Contours of the temperature in the rod at (a) 15 μs and (b) 30 μs computed with LS-DYNA.

begins to decrease. The axial velocity of points on the rear surface computed with the MSPH method is lower than that given by LS-DYNA. Hence the final length of the rod, 34.7 mm, computed with the MSPH code is slightly larger than the 34.5 mm given by both the axisymmetric and the 3-D analyses performed with LS-DYNA; see Fig. 4. Final lengths computed with the two codes agree very well with the experimentally found final length of 34.6 mm.

The impacted face of the rod and the region adjacent to it is mushroomed; time histories of the radius of the deformed impact face computed with the two codes are exhibited in Fig. 5. For each of the three solutions, this radius ceases to increase for times greater than 30 μs; the radius computed with the MSPH code is the smallest and that given by the 3-D analysis of the problem with LS-DYNA the largest; the two differ by about 6.0%. The maximum radii of the impacted face computed with the MSPH code, and the axisymmetric and the 3-D analyses with LS-DYNA equal, respectively, 4.99 mm, 5.31 mm and 5.31 mm. Each of these values is greater than the experimentally measured value of 4.75 mm.

Since the axisymmetric and the 3-D analyses with LS-DYNA give nearly identical results, henceforth we only give results of the axisymmetric analysis with LS-DYNA.

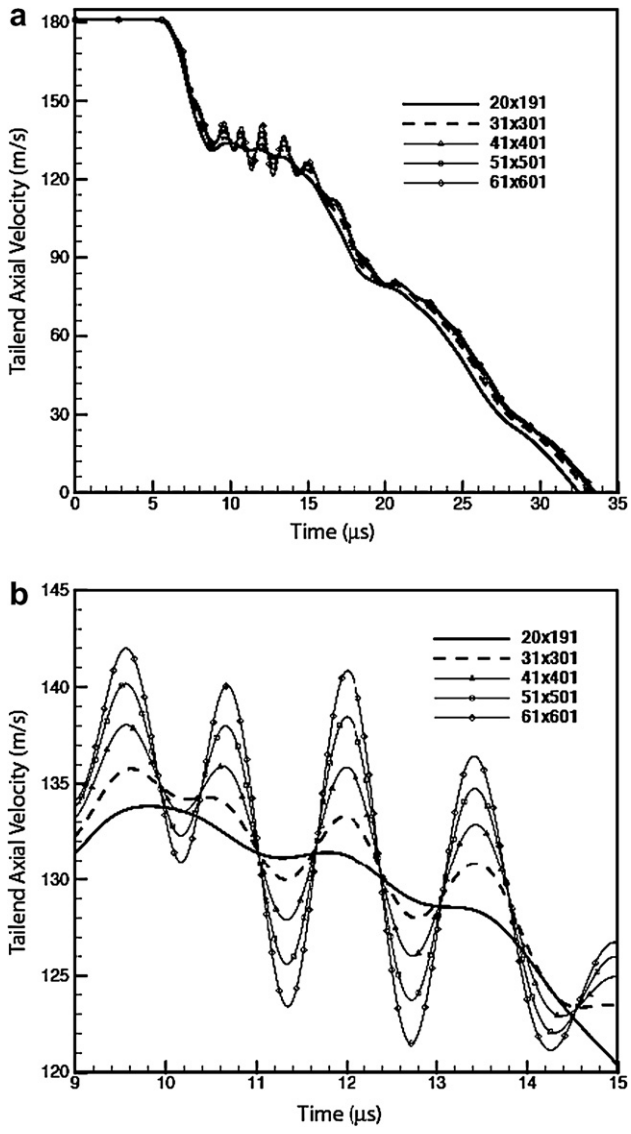

Fig. 10. Time histories of the tail end axial velocity computed by the MSPH method with five different distributions of particles.

Figs. 6 and 7 depict contours of the effective plastic strain at 15 μs and 30 μs after impact, for the MSPH and the LS-DYNA solutions. It is evident that at each time, the maximum effective plastic strain computed with LS-DYNA is a little higher than that with the MSPH code. The difference in the two peak values of the effective plastic strain equals 1% and 4%, respectively, at 15 μs and 30 μs. Fringe plots of the temperature field computed with the two codes, evinced in Figs. 8 and 9, look very similar. At time = 15 μs, the maximum temperature in the rod computed with LS-DYNA is 512.9 K, which is 5.4% higher than the 486.5 K given by the MSPH method, and at time = 30 μs, the difference between the maximum temperatures computed by the two methods is 7.6%. The spikes in the temperature near the centroidal axis of the rod computed with the LS-DYNA code have larger amplitudes than those computed with the MSPH code. It could be due to different basis functions and smoothing techniques employed in the MSPH code and the LS-DYNA. LS-DYNA employs one-point integration rule and uses hour-glass control to eliminate spurious modes of deformation.

4.2.1. Effect of the number of particles

Four additional discretizations, 31×301, 41×401, 51×501 and 61×601 (number of particles in the radial direction × number of particles in the axial direction) were used to compute results with the MSPH method.

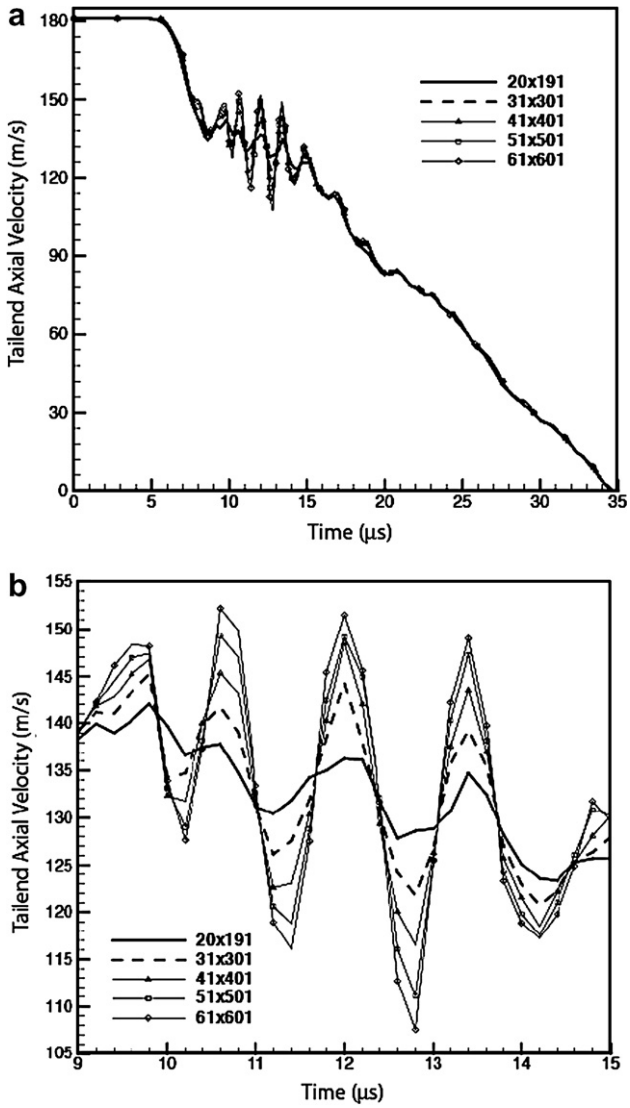

Fig. 11. Time histories of the tail end axial velocity computed with LS-DYNA with five different nodal distributions.

Fig. 10 exhibits the time history of the tail end axial velocity for the five cases that includes results for the 20×191 discretization. It can be seen that the tail end velocity increases with an increase in the number of particles, but the difference between any two sets of results is very small. However, the amplitude of oscillations in the tail end axial velocity increases with an increase in the number of particles; cf. Fig. 10b. The effect of the number of nodes is also studied by using LS-DYNA and results are given in Fig. 11. The difference in tail end velocities is much smaller, but the amplitude of oscillations is larger than that computed with the MSPH method. As for the MSPH method the amplitude of oscillations increases with an increase in the number of nodes. Thus the coarse distribution of nodes (or particles) smoothens out the oscillations.

The comparison of the development of the mushroomed end is given in Fig. 12. It is apparent that the radius of the mushroomed face increases with an increase in the number of particles. Also, the vertical dis-

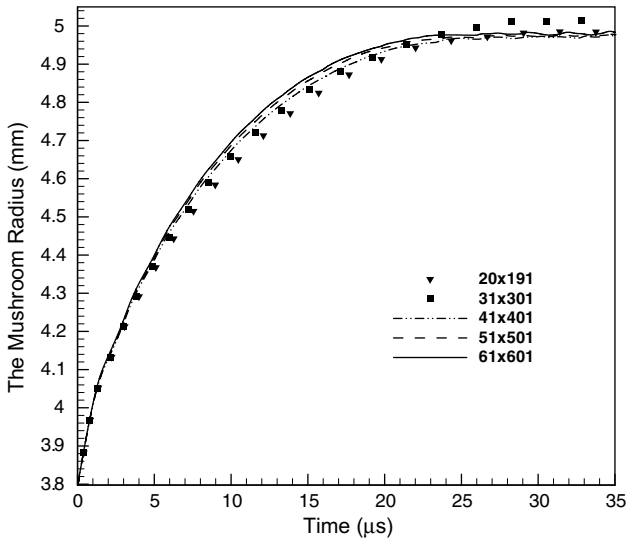

Fig. 12. For different numbers of particles time histories of the radius of the impacted face of the rod.

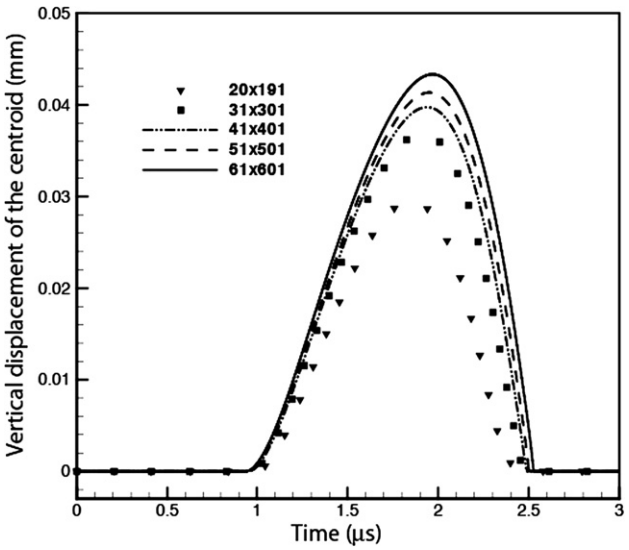

Fig. 13. For different number of particles, time histories of the vertical displacement of the centroid of the impact face for time less than 3 μs.

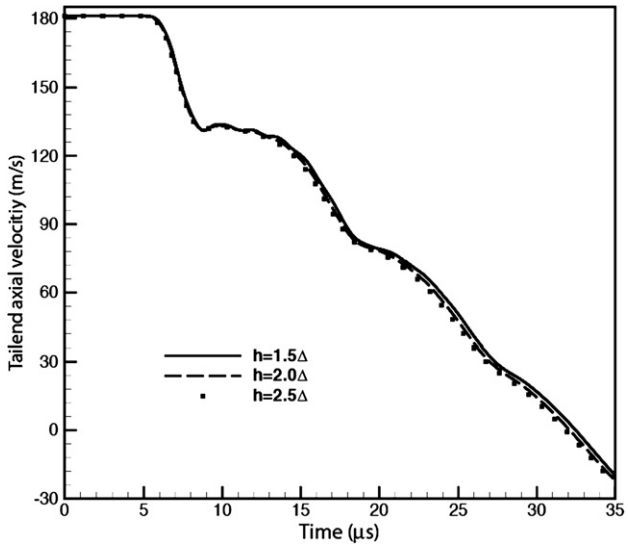

Fig. 14. Time histories of the tail end axial velocity computed by the MSPH method with three different values of the smoothing length.

placement of the particle at the centroid of the impact face increases with an increase in the number of particles; see Fig. 13.

An increase in the number of particles or nodes influences significantly the amplitude of vertical displacements of points near the centroid of the impacted face but has a negligible effect on the radius of the deformed impacted face and the final length of the rod.

Even though deformations of the material in the mushroomed region are inhomogeneous, involve peak strains of 84% and the maximum temperature of 500 K, the deformation was not found to localize into narrow regions of intense plastic deformation usually called adiabatic shear bands.

4.2.2. Effect of the smoothing length

The smoothing length h plays an important role in the MSPH method. A larger smoothing length will increase the number of particles in a particle's compact support and hence will increase the CPU time required for the analysis of the problem. On the other hand, a very small smoothing length will not include enough number of particles in a particle's compact support resulting in the matrix B in Eq. (2.3) becoming singular. Generally, the smoothing length is taken as 1.5 times the minimum distance between two adjacent particles, as we have done in our computations. Here we also give in Fig. 14 results for two other values of h, i.e., $h = 2.0\Delta$, and $h = 2.5\Delta$. It can be seen that the three values of the smoothing length give essentially the same time histories of the tail end axial velocity.

4.2.3. Effect of the coefficient α_{cs} in the smoothing function

Time histories of the tail end axial velocity for different values of the coefficient α_{cs} in the conservative smoothing function (3.23) are exhibited in Fig. 15. The tail end axial velocity increases with a decrease in the value of α_{cs}. It can be seen that the amplitude of oscillations increases with a decrease in the value of α_{cs}. From this aspect, conservative smoothing is similar to the artificial viscosity, i.e., small values of viscosity result in larger amplitudes of oscillation while a large value of viscosity smoothes out the solution. We note that results for $\alpha_{cs} = 0.2$, 0.3 and 0.4 are very close to each other implying thereby that results presented above do not have excessive damping.

5. Comparison with experimental results

We have simulated all twelve test configurations reported in [24] with the MSPH code by taking 20 particles in radial direction, while the particle number in axial direction is determined by the rod length so that the

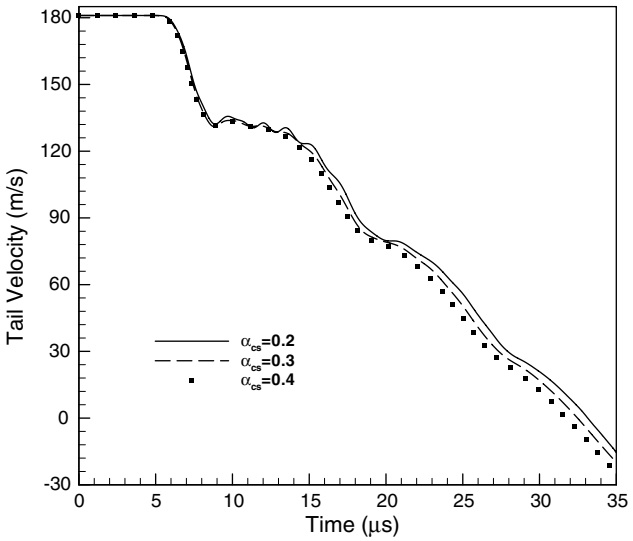

Fig. 15. Time histories of the tail end axial velocity computed by the MSPH method with three different values of the conservative smoothing coefficient.

Table 1
Comparison between experimental and computed values of different variables for the Taylor impact test on low strength 4340 steel rods

Test no.	Initial dia. (mm)	Initial length (mm)	Impact speed (m/s)	Final length (mm)		Final length of undeformed rod (mm)		Diameter of the impact face (mm)	
				Test	Simulation	Test	Simulation	Test	Simulation
1	7.595	11.39	285	9.2	9.6	3.2	2.7	10.9	10.3
2	7.595	15.19	234	13.1	13.3	5.6	5.3	10.2	10.1
3	7.595	15.19	275	12.4	12.8	5.2	4.7	11.2	10.7
4	7.595	15.19	302	12.0	12.5	5.2	4.3	12.2	11.1
5	7.595	25.29	170	23.4	23.3	11.2	10.4	9.2	9.5
6	7.595	25.29	215	22.4	22.5	10.0	10.0	10.3	10.4
7	7.595	37.97	181	34.6	34.6	15.5	17.0	9.5	10.0
8	7.595	37.97	183	34.7	34.6	15.3	17.0	9.8	10.0
9	7.595	37.97	224	33.0	33.3	11.9	15.5	10.5	11.0
10	7.595	37.97	234	33.1	32.9	13.3	15.0	10.6	11.2
11	7.595	37.97	270	31.3	32.0	11.8	12.9	12.1	11.8
12	7.595	56.96	242	47.8	48.7	17.5	22.0	11.6	11.6

particle distances in two directions are the same, $h = 1.5\Delta$, and $\alpha_{cs} = 0.2$. The computed final length of the rod, the diameter of the impact face, and the length of the undeformed region of the rod are compared with their corresponding experimental values in Table 1. The final undeformed length is defined as the length of the contiguous rod where the nominal radial strain is less than 0.2%. It can be seen that computed values of different quantities agree very well with their experimental counterparts. The maximum difference between the two final lengths is 4.3% and occurs for the configuration of test 1, and that between the final diameters of the impacted face is 9.0%.

6. Comparison of the MSPH code with LS-DYNA

The commercial code LS-DYNA is highly optimized and has different options to account for contact between two distinct bodies and smoothen out the solution. We used 8-node brick elements for the analysis of the 3-D problem and 4-node quadrilateral elements for studying the axisymmetric problem. In each case, the code uses one-point integration rule to evaluate integrals defined on an element, and eliminates spurious

modes by implementing the hour-glass control which is equivalent to introducing artificial viscosity. Whereas LS-DYNA employs displacement based formulation and assumes that stresses and temperatures are constants within each element, the MSPH code takes displacements, stresses and temperatures as unknowns. In LS-DYNA stresses and temperatures are computed only at the integration point that increases its efficiency. However, it necessitates using a very fine mesh to resolve regions of intense plastic deformation and regions with very high gradients of solution variables. Both codes use the radial return method to ensure that stresses satisfy the yield criterion, the Johnson-Cook viscoplasticity relation, and neglect effects of heat conduction. Our effort is focused on presenting the MSPH method rather than developing an optimum production code. We feel that it is not fair to compare the performance of a research code with that of a commercial code.

7. Remarks

We note that Batra and his colleagues [28–30] have used the code DYNA2D to analyze Taylor impact problems under different assumptions, but had not compared their research findings with test values as has been done here. They [31,32] have also analyzed with the FEM the localization of deformation into narrow regions of intense plastic deformation in heat-conducting thermo-elasto-viscoplastic materials.

We have also generalized the MSPH basis functions to symmetric smoothed particle hydrodynamics (SSPH) basis functions [33]. This method permits the use of a large variety of kernel functions, requires the inversion of a symmetric matrix to find the basis functions, and is thus computationally less expensive than the MSPH method.

8. Conclusions

The Modified Smoothed Particle Hydrodynamics (MSPH) method has been extended to the analysis of axisymmetric problems for thermoelastoviscoplastic materials. Results computed from it have been found to compare well with those obtained by analyzing either axisymmetric or three-dimensional deformations with the LS-DYNA code. The effect of the particle number, the smoothing length and the coefficient in the conservative smoothing function has also been studied. Results computed with the MSPH formulation for twelve configurations of the Taylor impact test are found to agree well with their corresponding experimental values. It has been found that the presently computed results match well with the experimental findings. An increase in either the total number of particles or the smoothing length improves the accuracy of results. The conservative smoothing employed herein has not introduced excessive damping in the numerical solution. The basis functions for the MSPH method are complete polynomials as are for the finite element method. Whereas in the MSPH method, the function and its derivatives can be approximated by using different basis functions and basis functions for the derivatives of a function are not obtained by differentiating those for the function itself, in the finite element method basis functions for the derivative of a function are usually obtained by differentiating those for the function. Advantages of a meshless method over the finite element method include the following. A meshless method (i) does not require element connectivity and thus saves time required to prepare the data input file, (ii) allows for cracks to propagate along paths dictated by the physics of the problem rather than a finite element mesh, (iii) allows for the analysis of phase transformations more readily than the finite element method, (iv) avoids difficulties associated with mesh distortion usually encountered in large deformation problems, and (v) permits accurate computations of fluxes (e.g. stresses, heat flux) at arbitrary points. As mentioned above, the MSPH method has the additional advantage of not having to differentiate shape functions to obtain derivatives of a function. It is not fair to compare the CPU time required by our research code with that needed by highly optimized commercial code LS-DYNA.

The MSPH basis functions provided herein can also be used in other meshless methods.

Acknowledgments

This work was partially supported by the ONR Grants N00014-1-98-0300 and N00014-1-06-0567 to Virginia Polytechnic Institute and State University (VPI&SU). Views expressed herein are those of authors and neither of the funding agency nor of VPI&SU.

References

[1] G.M. Zhang, R.C. Batra, Modified smoothed particle hydrodynamics method and its application to transient problems, Comput. Mech. 34 (2004) 137–146.
[2] R.C. Batra, G.M. Zhang, Analysis of adiabatic shear bands in elasto-thermo-viscoplastic materials by modified smoothed-particle hydrodynamics (MSPH) method, J. Comput. Phys. 201 (2004) 172–190.
[3] G.M. Zhang, R.C. Batra, Wave propagation in functionally graded materials by Modified Smoothed Particle Hydrodynamics (MSPH) method, J. Comput. Phys. 222 (2007) 374–390.
[4] R.C. Batra, G.M. Zhang, Search algorithm, and simulation of elastodynamic crack propagation by Modified Smoothed Particle Hydrodynamics (MSPH) method, Comput. Mech. 40 (2007) 531–546.
[5] L.B. Lucy, A numerical approach to the testing of the fission hypothesis, Astron. J. 82 (1977) 1013–1024.
[6] R.A. Gingold, J.J. Monaghan, Smoothed particle hydrodynamics: theory and application to non-spherical stars, Mon. Not. Roy Astron. Soc. 181 (1977) 375–389.
[7] L.D. Libersky, A.G. Petschek, Smooth particle hydrodynamics with strength of materials, advances in the free Lagrange method, Lect. Notes Phys. 395 (1990) 248–257.
[8] J.J. Monaghan, Simulating free surface flows with SPH, J. Comput. Phys. 110 (1994) 399–406.
[9] M.B. Liu, G.R. Liu, Z. Zhong, K.Y. Lam, Computer simulation of high explosive explosion using smoothed particle hydrodynamics methodology, Comput. Fluids 32 (3) (2003) 305–322.
[10] P.W. Randles, T.C. Carney, L.D. Libersky, J.D. Renick, A.G. Petschek, Calculation of oblique impact and fracture of tungsten cubes using smoothed particle hydrodynamics, Int. J. Impact Eng. 17 (1995) 661–672.
[11] D.F. Medina, J.K. Chen, Three-dimensional simulations of impact induced damage in composite structures using the parallelized SPH method, Composites Part A 31 (2000) 853–860.
[12] J.K. Chen, J.E. Beraun, C.J. Jih, An improvement for tensile instability in smoothed particle hydrodynamics, Comput. Mech. 23 (1999) 279–287.
[13] J.K. Chen, J.E. Beraun, C.J. Jih, Completeness of corrective smoothed particle method for linear elastodynamics, Comput. Mech. 24 (1999) 273–285.
[14] P.W. Randles, L.D. Libersky, Normalized SPH with stress points, Int. J. Numer. Methods Eng. 48 (2000) 1445–1462.
[15] R. Vignjevic, J. Campbell, L.D. Libersky, A treatment of zero-energy modes in the smoothed particle hydrodynamics method, Comput. Methods Appl. Mech. Eng. 184 (2000) 67–85.
[16] G.R. Johnson, E.H. Petersen, R.A. Stryk, Incorporation of an SPH option into the EPIC code for a wide range of high velocity impact computations, Int. J. Impact Eng. 14 (1993) 385–394.
[17] A.G. Petschek, L.D. Libersky, Cylindrical smoothed particle hydrodynamics, J. Comput. Phys. 109 (1993) 76–83.
[18] P.W. Randles, L.D. Libersky, Smoothed particle hydrodynamics: some recent improvements and applications, Comput. Methods Appl. Mech. Eng. 139 (1996) 375–408.
[19] D.L. Hicks, J.W. Swegle, S.W. Attaway, Conservative smoothing stabilizes discrete-numerical instabilities in SPH material dynamics computations, Appl. Math. Comput. 85 (1997) 209–226.
[20] D.L. Hicks, L.M. Liebrock, SPH hydrocodes can be stabilized with shape-shifting, Comput. Math. Appl. 38 (1999) 1–16.
[21] L.D. Libersky, P.W. Randles, T.C. Carney, D.L. Dickinson, Recent improvements in SPH modeling of hypervelocity impact, Int. J. Impact Eng. 20 (1997) 525–532.
[22] D.L. Hicks, L.M. Liebrock, Conservative smoothing with B-splines stabilizes SPH material dynamics in both tension and compression, Appl. Math. Comput. 150 (2004) 213–234.
[23] W.F. Noh, Errors for calculations of strong shocks using an artificial viscosity and an artificial heat flux, J. Comput. Phys. 72 (1978) 78–120.
[24] J.W. House, J.C. Lewis, P.P. Gillis, L.L. Wilson, Estimation of flow stress under high rate plastic deformation, Int. J. Impact Eng. 16 (1995) 189–200.
[25] W.K. Rule, A numerical scheme for extracting strength model coefficients from Taylor test data, Int. J. Impact Eng. 19 (1997) 797–810.
[26] R.C. Batra, C.H. Kim, Effect of thermal conductivity on the initiation, growth and band width of adiabatic shear bands, Int. J. Eng. Sci. 29 (1991) 949–960.
[27] R.C. Batra, M.H. Lear, Adiabatic shear banding in plane strain tensile deformations of eleven thermoelastoviscoplastic materials with finite thermal wave speed, Int. J. Plasticity 21 (2005) 1521–1545.
[28] J.B. Stevens, R.C. Batra, Adiabatic shear band in the Taylor impact test for a WHA rod, Int. J. Plasticity 14 (1998) 841–854.
[29] R.C. Batra, J.B. Stevens, On the L/D effect in the Taylor impact test, in: S.N. Atluri, G. Yagawa (Eds.), Advances in Computational Engineering Science, Tech Science Press, Forsyth, Georgia, 1997, pp. 1134–1139.
[30] R.C. Batra, J.B. Stevens, Adiabatic shear bands in axisymmetric impact and penetration problems, Comp. Meth. Appl. Mech. Engrg. 151 (1998) 325–342.
[31] R.C. Batra, K.I. Ko, Analysis of shear bands in dynamic axisymmetric compression of a thermoviscoplastic cylinder, Int. J. Eng. Sci. 31 (1993) 529–547.
[32] R.C. Batra, B.M. Love, Mesoscale analysis of shear bands in high strain rate deformations of tungsten/nickel-iron composites, J. Therm. Stress. 28 (2005) 747–782.
[33] R.C. Batra, G.M. Zhang, SSPH basis functions for meshless methods, and comparison of solutions with strong and weak formulations, Comput. Mech. 41 (2008) 527–545.